

Time-Dependent Relativistic Two-Component Equation-of-Motion Coupled-Cluster for Open-Shell Systems: TD-EA/IP-EOMCC

P. D. Varuna S. Pathirage, Stephen H. Yuwono, and A. Eugene DePrince III^{a)}

Department of Chemistry and Biochemistry, Florida State University, Tallahassee, FL 32306-4390

We present a combined imaginary-time/real-time time-dependent (TD) approach for evaluating linear absorption spectra of open-shell systems at the electron attachment (EA) and ionization potential (IP) equation-of-motion coupled-cluster (EOMCC) levels of theory and within the exact two-component relativistic framework. The absorption lineshape is given by the Fourier transform of the electric dipole autocorrelation function, which is obtained from a real-time simulation. Approximations of the lowest-energy EA- and IP-EOMCC eigenstates, which are required as initial states for the real-time simulation, are generated by propagating a Koopman EA/IP state in imaginary time. TD-EA/IP-EOMCC linear absorption spectra of open-shell atomic systems (Na, K, Rb, F, Cl, and Br) closely reproduce those obtained from standard TD-EA/IP procedures carried out in the frequency domain. We find that the existence of low-lying states with non-negligible overlap with the Koopman determinant impacts the length of the imaginary-time propagation required to obtain an initial state that produces correct absolute energies and peak height intensities in spectra extracted from the subsequent real-time TD-EA/IP-EOMCC calculations.

I. INTRODUCTION

Real-time (RT) time-dependent (TD) electronic structure methods^{1,2} have enjoyed an increase in popularity in recent years because of their usefulness in describing wide-ranging excited-state processes relevant to ultrafast dynamical phenomena,^{3–7} various spectroscopic signals,^{8–20} and time-resolved optical experiments.^{17,21–26} RT-TD approaches also exhibit some desirable practical benefits over frequency-domain representations of excited-state electronic structure. For example, RT-TD methods can be used to obtain broad spectral information in large systems with high densities of states with a significantly reduced memory footprint,^{8,11} as compared to their frequency-domain counterparts. Frequency-domain calculations built on iterative eigen-solver techniques may require the storage of many wavefunction-sized objects, whereas RT-TD methods require the storage of only a few such objects. The reduced-storage requirement is particularly desirable for correlated many-body methods such as coupled-cluster (CC) or equation-of-motion (EOM) CC theory.

In the context of time-independent electronic structure theory, CC^{27–33} and EOMCC^{34–36} are regarded as “gold standard” methods that effectively balance the accurate treatment of electron correlation effects and computational cost. Indeed, the basic CC approach with single and double excitations (CCSD) and its EOMCCSD counterpart can usually provide qualitatively correct descriptions of electronic structure,^{36–38} and the inclusion of higher-order many-body components of the cluster and EOM excitation operators, as is done in CC/EOMCC with up to triple excitations (CCSDT/EOMCCSDT)^{39–42} or CC/EOMCC with up to quadruple excitations (CCSDTQ/EOMCCSDTQ)^{43–46} results in a hierarchy of CC/EOMCC methods that quickly converges to the full configuration interaction (CI) solution.³³ Given the successes of CC and EOMCC, it is not surprising that several

TD formulations of CC^{47–56} and EOMCC^{9,11,12,15,20,26,50,57–60} have been put forward.

In this work, we focus on the application of moment-based TD-EOMCC approaches^{9,11,12,20} to the description of open-shell species. The simplest route to spectra of such species would be the direct application of TD-EOMCC to the open-shell states obtained using either unrestricted or restricted open-shell Hartree–Fock reference (abbreviated as UHF and ROHF, respectively). However, it is well known that UHF-based calculations often break total spin (\hat{S}^2) symmetry, while ROHF-based calculations are not invariant with respect to the canonicalization of the Fock matrix. Within the EOMCC framework, these problems can be avoided by relying on non-particle-conserving operators characterizing the ionization potential (IP)^{61–70} and electron attachment (EA)^{68–73} EOMCC approaches. Unlike in the conventional particle-conserving EOMCC (also known as electron-excitation (EE) EOMCC), IP-EOMCC removes an electron from and EA-EOMCC add an electron to a reference wave function. If this reference is an \hat{S}^2 eigenfunction (*i.e.*, a restricted Hartree–Fock [RHF] reference), then the resulting open-shell description can maintain rigorous spin adaptation, allowing one to describe radical species with the proper degeneracy structures. To the best of our knowledge, the utility of non-particle-conserving EOMCC *ansatze* such as EA/IP-EOMCC in the context of TD-EOMCC remains unexplored.

This paper is organized as follows. In Sec. II, we lay out the pertinent details of EA/IP-EOMCC and describe the extension of these methods to the time domain. We also discuss the generation of suitable initial states for moment-based TD-EA/IP-EOMCC (*i.e.*, approximations to the lowest-energy EA/IP-EOMCC eigenfunctions) via imaginary time propagation, as opposed to solving the ground-state EA/IP-EOMCC eigenvalue problems. Section III then provides the details of the calculations performed in this work, the results of which are presented in Sec. IV. As test cases, we compute the linear absorption spectra of the group I alkali metals (Na, K, and Rb) and group VII halogen atoms (F, Cl, and Br). These systems exhibit non-negligible spin-orbit coupling (SOC) effects, which we describe within the exact two-component

^{a)}Electronic mail: adeprince@fsu.edu

(X2C) relativistic framework. We also explore the sensitivity of the spectra to the quality of the initial state generated via the imaginary time propagation. Lastly, Sec. V provides an overall summary of the work and some concluding remarks.

II. THEORY

A. The EA/IP-EOMCCSD formalism

We begin by summarizing the IP- and EA-EOMCC formalism, focusing on the EA/IP-EOMCCSD level of theory. The starting point of these methodologies is the CCSD description of a closed-shell reference state, where the wave function is given by

$$|\Psi_0^{(N)}\rangle = \exp(\hat{T})|\Phi\rangle \quad (1)$$

Here, \hat{T} is the CCSD cluster operator and $|\Phi\rangle$ is an N -electron RHF reference determinant. The cluster operator can be expressed as a many-body expansion, which, for CCSD, is given by

$$\hat{T} = \hat{T}_1 + \hat{T}_2 = t_a^i \hat{a}^a \hat{a}_i + \frac{1}{4} t_{ab}^{ij} \hat{a}^a \hat{a}^b \hat{a}_j \hat{a}_i. \quad (2)$$

In Eq. 2, t_a^i and t_{ab}^{ij} are the singles (or 1-particle–1-hole, 1p–1h) and doubles (or 2-particle–2-hole, 2p–2h) cluster amplitudes, respectively, and \hat{a}_p (\hat{a}^p) is a fermionic annihilation (creation) operator acting on the spin orbital labeled p . In this work, we use the usual notation where i, j, \dots and a, b, \dots are used for labeling spin orbitals that are occupied and unoccupied, respectively, in $|\Phi\rangle$, while the labels p, q, \dots are used for spin orbitals with generic occupancy. We also employ the Einstein convention, in which repeated upper and lower indices imply summation. The cluster amplitudes are determined by solving the system of non-linear equations

$$\langle \Phi_i^a | \bar{H} | \Phi \rangle = \langle \Phi_{ij}^{ab} | \bar{H} | \Phi \rangle = 0, \quad (3)$$

where $\bar{H} = \exp(-\hat{T})\hat{H}\exp(\hat{T})$ is the CCSD similarity-transformed Hamiltonian and $|\Phi_i^a\rangle$ and $|\Phi_{ij}^{ab}\rangle$ are singly and doubly substituted determinants, respectively. Subsequently, we evaluate the ground-state energy as

$$E_0^{(N)} = \langle \Phi | \bar{H} | \Phi \rangle. \quad (4)$$

To access the $(N \pm 1)$ -electron states, we employ non-particle-conserving EOM operators on top of the N -electron wave function as

$$|\Psi_K^{(N\pm 1)}\rangle = \hat{R}_K^{(\pm 1)}|\Psi_0^{(N)}\rangle = \hat{R}_K^{(\pm 1)}\exp(\hat{T})|\Phi\rangle, \quad (5)$$

where the $\hat{R}_K^{(\pm 1)}$ operator is defined as

$$\hat{R}_K^{(\pm 1)} = \hat{R}_{K,1}^{(\pm 1)} + \hat{R}_{K,2}^{(\pm 1)} = r_a(K)\hat{a}^a + \frac{1}{2}r_{ab}^j(K)\hat{a}^a \hat{a}^b \hat{a}_j, \quad (6)$$

in the case of EA-EOMCCSD, and

$$\hat{R}_K^{(-1)} = \hat{R}_{K,1}^{(-1)} + \hat{R}_{K,2}^{(-1)} = r^i(K)\hat{a}_i + \frac{1}{2}r_b^{ij}(K)\hat{a}^b \hat{a}_j \hat{a}_i, \quad (7)$$

in the case of IP-EOMCCSD. Note that, unlike the cluster operator, the EA-EOM operators are of the np - $(n-1)h$ excitation type, and the IP-EOM many-body components are of the $(n-1)p$ - nh type. Additionally, because our targets are the spectra of the $(N \pm 1)$ -electron radical species, we will use $K = 0$ to refer to the ground state of the open-shell species, which should not be confused with the CCSD wave function $|\Psi_0^{(N)}\rangle$. The $(N \pm 1)$ -electron spectrum could be obtained by solving the eigenvalue problem

$$\bar{H}_N \hat{R}_K^{(\pm 1)} |\Phi\rangle = \omega_K^{(N\pm 1)} \hat{R}_K^{(\pm 1)} |\Phi\rangle, \quad (8)$$

where $\bar{H}_N = \bar{H} - E_0^{(N)}$ and $\omega_K^{(N\pm 1)} = E_K^{(N\pm 1)} - E_0^{(N)}$ correspond to the EA [$\omega_K^{(N+1)}$] and IP [$\omega_K^{(N-1)}$] energies relative to the N -electron reference state. To avoid confusion, we use the symbol ω_K without the $(N \pm 1)$ superscript to denote excitation energies with respect to the relevant lowest-energy $(N \pm 1)$ -electron state (*i.e.*, $\omega_K = E_K^{(N\pm 1)} - E_0^{(N\pm 1)}$).

The similarity transformation of the Hamiltonian results in a loss of Hermiticity, which means that the left- and right-hand eigenvectors of \bar{H} are not Hermitian conjugates of one another (*i.e.*, $\langle \Psi_K | \neq |\Psi_K \rangle^\dagger$). Thus, if properties other than energy are of interest, one must solve the left-hand eigenvalue problem for the left-hand wave functions as well. In the EA/IP-EOMCCSD framework, the left-hand wave function is parameterized as

$$\langle \tilde{\Psi}_K^{(N\pm 1)} | = \langle \Phi | \hat{L}_K^{(\pm 1)} \exp(-\hat{T}), \quad (9)$$

where we have introduced the EOM de-excitation operators

$$\hat{L}_K^{(\pm 1)} = \hat{L}_{K,1}^{(\pm 1)} + \hat{L}_{K,2}^{(\pm 1)} = l^a(K)\hat{a}_a + \frac{1}{2}l_j^{ab}(K)\hat{a}^j \hat{a}_b \hat{a}_a, \quad (10)$$

in the case of EA-EOMCCSD, and

$$\hat{L}_K^{(-1)} = \hat{L}_{K,1}^{(-1)} + \hat{L}_{K,2}^{(-1)} = l_i(K)\hat{a}^i + \frac{1}{2}l_{ij}^b(K)\hat{a}^i \hat{a}^j \hat{a}_b, \quad (11)$$

in the case of IP-EOMCCSD. The left-hand EA/IP-EOM amplitudes are obtained by solving the left-hand eigenvalue problem

$$\langle \Phi | \hat{L}_K^{(\pm 1)} \bar{H}_N = \omega_K^{(N\pm 1)} \langle \Phi | \hat{L}_K^{(\pm 1)}, \quad (12)$$

and the left- and right-hand eigenvectors form a biorthonormal set, *i.e.*, they satisfy the relationship

$$\langle \tilde{\Psi}_K^{(N\pm 1)} | \Psi_L^{(N\pm 1)} \rangle = \langle \Phi | \hat{L}_K^{(\pm 1)} \hat{R}_L^{(\pm 1)} | \Phi \rangle = \delta_{KL}, \quad (13)$$

where δ_{KL} is the Kronecker delta. Properties and transition properties between EA/IP-EOMCCSD states can then be computed as

$$\langle \hat{\Omega} \rangle_{KL} = \langle \tilde{\Psi}_K^{(N\pm 1)} | \hat{\Omega} | \Psi_L^{(N\pm 1)} \rangle = \langle \Phi | \hat{L}_K^{(\pm 1)} \bar{\Omega} \hat{R}_L^{(\pm 1)} | \Phi \rangle, \quad (14)$$

where $\bar{\Omega} = \exp(-\hat{T})\hat{\Omega}\exp(\hat{T})$ is the similarity-transformed form of the operator of interest $\hat{\Omega}$.

B. Extension of EA/IP-EOMCCSD to the time-domain

In this subsection, we extend the TD-EOMCC formalism described in Refs. 9,11,12,20 to the EA/IP-EOMCC domain. Again, we focus on the EA/IP-EOMCCSD levels of theory, but the formalism presented here can be extended to higher levels. Focusing on the linear absorption spectra of radicals, our starting point is the isotropically averaged oscillator strength

$$f(\omega) = \frac{2}{3} \omega \sum_{\alpha} \text{Re}\{[I_{\alpha}(\omega)]\}, \quad (15)$$

where ω is a frequency, α is a cartesian component, and $I_{\alpha}(\omega)$ is the lineshape function for a given direction in the cartesian coordinate. The lineshape function is given by the Fourier transformation

$$I_{\alpha}(\omega) = \mathcal{F} \left[e^{-\gamma|t|} \langle \tilde{M}_{\hat{\mu}}^{\alpha, (N\pm 1)} | \hat{U}(t) | M_{\hat{\mu}}^{\alpha, (N\pm 1)} \rangle \right], \quad (16)$$

where γ is a Lorentzian broadening factor, t is time, and $\hat{U}(t) = e^{i\tilde{H}_N t}$. The EA/IP-EOMCC moment functions entering the Fourier transformation, which serve as the initial states in the propagation, are defined as

$$|M_{\hat{\mu}}^{\alpha, (N\pm 1)}\rangle = \bar{\mu}_{\alpha} \hat{R}_0^{(\pm 1)} |\Phi\rangle \quad (17)$$

and

$$\langle \tilde{M}_{\hat{\mu}}^{\alpha, (N\pm 1)} | = \langle \Phi | \hat{L}_0^{(\pm 1)} \bar{\mu}_{\alpha}, \quad (18)$$

in which $\bar{\mu}_{\alpha} = \exp(-\hat{T}) \hat{\mu}_{\alpha} \exp(\hat{T})$ is the similarity-transformed α cartesian component of the dipole moment operator in the length gauge. As discussed in Ref. 20, this moment-based formalism can be generalized for other operators and types of linear spectra, but, in this work, we focus on the electric dipole moment operator relevant to electronic linear absorption. Furthermore, the time propagation operator, $\hat{U}(t)$, can be applied to either the bra or ket moment functions; this formalism allows us to propagate just one of them, which is a considerable savings compared to the need to propagate both left- and right-hand functions as is done in field-driven TD-EOMCC simulations.

The left- and right-hand moment functions can be expressed using many-body expansions and the operators introduced above to represent the lowest-energy ($K = 0$) left- and right-hand EA/IP-EOMCCSD wave functions. In the EA-EOMCCSD case, the right- and left-hand amplitudes are defined as

$$\begin{aligned} m_a(\alpha) &= \langle \Phi^a | \bar{\mu}_{\alpha} \hat{R}_0^{(+1)} | \Phi \rangle \\ m_{ab}^j(\alpha) &= \langle \Phi^a | \bar{\mu}_{\alpha} \hat{R}_0^{(+1)} | \Phi_j^b \rangle \end{aligned} \quad (19)$$

and

$$\begin{aligned} \tilde{m}^a(\alpha) &= \langle \Phi | \hat{L}_0^{(+1)} \bar{\mu}_{\alpha} | \Phi^a \rangle \\ \tilde{m}_j^{ab}(\alpha) &= \langle \Phi | \hat{L}_0^{(+1)} \bar{\mu}_{\alpha} | \Phi_j^b \rangle, \end{aligned} \quad (20)$$

respectively. In Eqs. 20 and 19, $|\Phi^a\rangle$ and $|\Phi_j^b\rangle$ are 1p and 2p-1h determinants, respectively, that span the EA-EOMCCSD excitation space. Similarly, the amplitudes for IP-EOMCCSD moment functions are given by

$$\begin{aligned} m^i(\alpha) &= \langle \Phi_i | \bar{\mu}_{\alpha} \hat{R}_0^{(-1)} | \Phi \rangle \\ m_b^{ij}(\alpha) &= \langle \Phi_{ij}^b | \bar{\mu}_{\alpha} \hat{R}_0^{(-1)} | \Phi \rangle \end{aligned} \quad (21)$$

and

$$\begin{aligned} \tilde{m}_i(\alpha) &= \langle \Phi | \hat{L}_0^{(-1)} \bar{\mu}_{\alpha} | \Phi_i \rangle \\ \tilde{m}_{ij}^b(\alpha) &= \langle \Phi | \hat{L}_0^{(-1)} \bar{\mu}_{\alpha} | \Phi_{ij}^b \rangle, \end{aligned} \quad (22)$$

in which $|\Phi_i\rangle$ and $|\Phi_{ij}^b\rangle$ are the 1h and 1p-2h determinants, respectively, spanning the IP-EOMCCSD excitation space. It is worth noting that these amplitudes are practically identical to a typical “sigma build” expressions characterizing the EA/IP-EOMCCSD diagonalization procedure, except for the use of $\bar{\mu}$ elements instead of those of \tilde{H} . Thus, one can use a minimally modified EA/IP-EOMCCSD machinery to prepare the initial $|M_{\hat{\mu}}^{\alpha, (N\pm 1)}\rangle$ and $\langle \tilde{M}_{\hat{\mu}}^{\alpha, (N\pm 1)} |$ states, and subsequently perform the propagation $\hat{U}(t) |M_{\hat{\mu}}^{\alpha, (N\pm 1)}\rangle$ [or $\langle \tilde{M}_{\hat{\mu}}^{\alpha, (N\pm 1)} | \hat{U}(t)$] using, for example, a Runge–Kutta-type time integration with the usual EA/IP-EOMCCSD sigma builds combined with the m or \tilde{m} amplitudes.

At this point, we highlight the primary differences between the TD-EA/IP-EOMCC formalism outlined above and its EE predecessor introduced in Ref. 9. In TD-EE-EOMCC, the initial moment functions are generated by the application of the similarity-transformed dipole operator on the N -electron CC ground state and its left-hand lambda counterpart. This structure implies that one only needs to solve for the usual lambda equations after obtaining the converged cluster amplitudes and ground-state CC energy in order to initialize TD-EE-EOMCC simulation. In contrast, within the TD-EA/IP-EOMCC framework, the moment functions cannot be evaluated without knowledge of the ground-state left- and right-hand wave functions of the open-shell system, which correspond to the lowest-energy state in the $(N \pm 1)$ -electron Hilbert space (or subspace defined by the EA/IP-EOMCC truncation level). A second distinction lies in the fact that the normal-ordered similarity-transformed Hamiltonian that appears in the time evolution operator, $\hat{U}(t) = e^{i\tilde{H}_N t}$, should be defined with respect to the ionized/electron attached state, *i.e.*, $\tilde{H}_N = \tilde{H} - E_0^{(N\pm 1)}$. Thus, initializing the TD-EA/IP-EOMCC procedure requires one to (i) solve the N -electron CCSD problem and (ii) determine the lowest-energy and left- and right-hand EA/IP-EOMCC, along with the associated energy.

In this work, we propose that one may employ imaginary time propagation to obtain the lowest-energy eigenpair within the $(N \pm 1)$ -electron Hilbert space. This procedure serves as an alternative to the direct solution of the left- and right-hand EA/IP-EOMCC eigenvalue problems. We begin by choosing a single $(N \pm 1)$ -electron determinant (*i.e.*, a Koopman state), and evolving this state according to

$$\lim_{\tau \rightarrow \infty} |\Psi_0^{(N\pm 1)}(\tau)\rangle = \lim_{\tau \rightarrow \infty} \exp(-\tilde{H}\tau) |\Phi^{(N\pm 1)}\rangle \quad (23)$$

and

$$\lim_{\tau \rightarrow -\infty} \langle \tilde{\Psi}_0^{(N\pm 1)}(\tau) \rangle = \lim_{\tau \rightarrow -\infty} \langle \Phi^{(N\pm 1)} \rangle \exp(\bar{H}\tau), \quad (24)$$

with $\tau = -it$. Here, $|\Phi^{(N+1)}\rangle = |\Phi^a\rangle$ where a is the lowest unoccupied spin orbital, and $|\Phi^{(N-1)}\rangle = |\Phi_i\rangle$ where i is the highest occupied spin orbital. In practice, one need not propagate to $\tau \rightarrow \infty$; rather, one may stop the simulation once the energy, $E_0^{(N\pm 1)}(\tau) = \langle \tilde{\Psi}_0^{(N\pm 1)}(\tau) | \bar{H} | \tilde{\Psi}_0^{(N\pm 1)}(\tau) \rangle$, changes by less than some predetermined threshold between successive time steps. Additionally, at every imaginary time step, it is necessary to ensure that binormality (*i.e.*, $\langle \tilde{\Psi}_0^{(N\pm 1)} | \tilde{\Psi}_0^{(N\pm 1)} \rangle = 1$) is enforced.

III. COMPUTATIONAL DETAILS

All CCSD, frequency-domain EA/IP-EOMCCSD, and TD-EA/IP-EOMCCSD calculations were carried out using an in-house Python code developed with the assistance of the p[†]q automated code generation package.^{74,75} The relativistic treatment used in this work was the one-electron X2C (1eX2C) approach; 1eX2C Fock matrices were obtained from the Chronus Quantum⁷⁶ electronic structure package. Non-relativistic two-electron integrals were obtained from the Psi4⁷⁷ quantum chemistry package. The Fock matrices and two-electron integral tensors were transformed to the molecular spinor basis using spinor coefficient matrices obtained from Chronus Quantum. To facilitate the transfer of matrices between Chronus Quantum and our (TD-)EA/IP-EOMCCSD code and streamline code verification, we opted to not include the two-electron SOC effects via screened-nuclei spin-orbit scaling that is usually included in 1eX2C calculations. The correctness of the resulting code and workflow were verified numerically against the 1eX2C-based EA/IP-EOMCCSD implementations in Chronus Quantum⁷⁶ and the RHF-based non-relativistic EA/IP-EOMCCSD code in GAMESS.^{68,70,78,79} All calculations were carried out using the x2c-SVPall-2c⁸⁰ basis sets obtained from Basis Set Exchange website.⁸¹

Group I alkali metals (Na, K, and Rb atoms) were treated at the EA-EOMCCSD level of theory, starting from the relevant cation references (Na⁺, K⁺, and Rb⁺ cations). Group VII halogen species (F, Cl, and Br atoms) were treated at the IP-EOMCCSD level of theory, starting from the relevant anion references (F⁻, Cl⁻, and Br⁻). All of the cation and anion reference systems are closed-shell species, so EA/IP-EOMCCSD yield atomic spectra that recover the correct degeneracy structures (*i.e.*, they correspond to spin-adapted results in the non-relativistic limit).

CCSD calculations were carried out in the molecular spinor basis. Frequency-domain EA/IP-EOMCCSD calculations were carried out by constructing and diagonalizing the full \bar{H} matrix in the space of 1p and 2p-1h excitations (for EA-EOMCCSD) or 1h and 1p-2h excitations (for IP-EOMCCSD). We correlated all occupied and virtual orbitals for the Na⁺ and F⁻ reference systems. For the K⁺ and Cl⁻ reference ions, we used the frozen-core approximation with

the innermost core spin orbitals frozen (1s). For the Rb⁺ and Br⁻ reference species, we froze ten core spin orbitals (the [Ne] core). Furthermore, in the case of Rb⁺, the 40 highest-energy virtual orbitals were also frozen.

For TD simulations, we generated initial states for real-time propagation via imaginary-time evolution of Koopman EA/IP states, using a time step of $d\tau = 0.01$ a.u. and a total simulation time of up to $\tau = 10$ a.u. Of course, the real-time simulations could be carried out in the spinor Slater determinant basis, but we chose the diagonal \bar{H} representation in order to use an exact time integration scheme and avoid potential artifacts stemming from approximate numerical integration. The real-time TD simulations used a time step of $dt = 0.01$ a.u. and a total propagation time of 10000 a.u. (≈ 242 fs). For the Fourier transformation of the dipole autocorrelation function [cf. Eq. 16], we used a Lorentzian damping factor of $\gamma = 5 \times 10^{-4}$ a.u., which corresponds to full-width at half maximum (FWHM) of 27.2 meV. We also padded the time-domain signal with zeroes to obtain a total of 2²³ points, resulting in frequency-domain spectra with $d\omega = 7.5 \times 10^{-5}$ E_h (≈ 2 meV). In order to resolve the SOC-induced splitting of peaks, we performed additional longer real-time TD-EA/IP-EOMCCSD simulations with a total propagation time of 671000 a.u. (about 16.23 ps) with the same time step of $dt = 0.01$ a.u., and applied a damping factor of $\gamma = 1.5 \times 10^{-5}$ a.u. (*i.e.*, a FWHM of 0.816 meV). In order to compare the peak heights the time signal is transformed with Riemann-sum approximation as shown below.

$$F(\omega) = \sum_{k=0}^{N-1} y(t_k) e^{-i\omega t_k} \Delta t, \quad (25)$$

where $y(t_n)$ is the time signal at time t_n and $\Delta t = t_{n+1} - t_n$.

IV. RESULTS AND DISCUSSION

Recall from Eqs. 17 and 18 that the initial moment functions for TD-EA/IP-EOMCC simulations require knowledge of the ground-state right-hand and left-hand eigenfunctions in the ionized/electron-attached excitation manifolds. These states could be determined as the lowest-energy solutions to the right-hand and left-hand EA/IP-EOMCC eigenvalue problems (Eqs. 8 and 12, respectively). On the other hand, as noted in Sec. II, one could obtain approximations to these states via imaginary time propagation. A question then emerges: how does the convergence of these approximate initial states impact spectra obtained from the subsequent real-time simulations? The accuracy of simulated linear absorption spectra corresponding to approximate initial states could be quantified in three ways: (i) absolute peak positions, (ii) relative peak positions, and (iii) relative peak intensities. The quality of the absolute peak positions will depend on the degree to which the energy associated with $|\Psi_0^{(N\pm 1)}(\tau)\rangle$ agrees with the true ground-state energy of the ($N \pm 1$)-electron states, which is dictated by the energy convergence achieved in the imaginary-time simulation used for state preparation because $E_0^{(N\pm 1)}$ enters the propagator for the real-time simulation through

TABLE I. Absolute values of the overlap between Koopman states and target EA/IP-EOMCCSD ground states (0) and between the Koopman states and the next lowest state with the same symmetry as the ground state (K), along with the excitation energy to state K (ω_K) in eV. For each set of degenerate states, only the largest overlap is shown.

Atom	$ \langle \Phi^{(N\pm 1)} \Psi_0^{(N\pm 1)} \rangle $	$ \langle \tilde{\Psi}_0^{(N\pm 1)} \Phi^{(N\pm 1)} \rangle $	$ \langle \Phi^{(N\pm 1)} \Psi_K^{(N\pm 1)} \rangle $	$ \langle \tilde{\Psi}_K^{(N\pm 1)} \Phi^{(N\pm 1)} \rangle $	ω_K
Na	0.9997	0.9998	0.0003	0.0002	4.2459
K	0.9967	0.9965	0.0416	0.0417	2.6452
Rb	0.9970	0.9964	0.0117	0.0116	2.4722
F	0.6652	0.7141	0.0006	0.0006	38.9892
Cl	0.6861	0.6862	0.0009	0.0008	29.0011
Br	0.7394	0.7125	0.0027	0.0024	23.2460

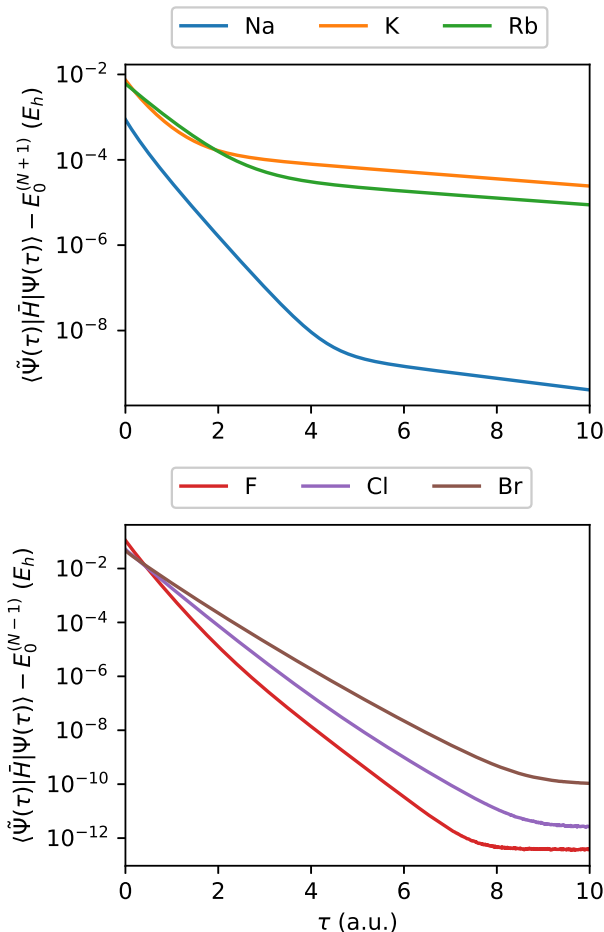


FIG. 1. Energy convergence for group I atoms with EA-EOMCCSD (top) and group VII atoms with IP-EOMCCSD (bottom).

$\tilde{H}_N = \tilde{H} - E_0^{(N\pm 1)}$. On the other hand, relative positions of the spectral features among themselves will be independent of τ because $E_0^{(N\pm 1)}$ in the propagator serves only to define zero in the excitation spectrum and does not impact relative excitation energies. Like the absolute peak positions, relative peak intensities will also depend on the quality of the initial state.

We can address the accuracy in absolute peak positions by

assessing the convergence of the energy associated with the approximate EA/IP-EOMCC ground state, $|\Psi_0^{(N\pm 1)}(\tau)\rangle$, as a function of the imaginary time parameter, τ . Figure 1 depicts the difference between the energy associated with $|\Psi_0^{(N\pm 1)}(\tau)\rangle$ and that of the relevant ground-state energy of the $(N \pm 1)$ -electron systems. Data are provided for the group I alkali metal atoms in the top panel (computed via EA-EOMCCSD) and group VII halogen atoms in the bottom panel (computed via IP-EOMCCSD). For the halogen atoms, we observe rapid convergence of the energy in the first 10 a.u. of imaginary time; at $\tau = 10$ a.u., the energy error in the bottom panel of Fig. 1 is $\approx 10^{-10} E_h$, or smaller. The story is slightly different for the alkali metal atoms. For the Na atom, we observe rapid convergence until $\tau \approx 4$ a.u., followed by slower convergence behavior; by $\tau = 10$ a.u., the energy is converged to less than 10^{-9} a.u. The energy associated with the approximate ground states of the K and Rb atoms converges much more slowly; at $\tau = 10$ a.u., the energy is only accurate to about $10^{-5} E_h$. Data in the Supporting Information show that the energy continues to converge for these systems, over several tens of a.u. By roughly $\tau = 30.0$ a.u., the energies associated with $|\Psi_0^{(N-1)}(\tau)\rangle$ for K and Rb are converged to within a microhartree of the respective ground-state energies. As for the quality of resulting spectra of the $(N \pm 1)$ -electron states, we can expect errors in absolute peak positions to mirror the errors depicted in Fig. 1; the largest of these errors at $\tau = 10.0$ a.u. are on the order of $10^{-5} E_h$ or ≈ 0.3 meV, which is well within the intrinsic error associated with the EA/IP-EOMCCSD level of theory.

The convergence behavior depicted in Fig. 1 can be understood from the degree to which the initial Koopman state and various open-shell eigenstates of \tilde{H} overlap, as well as the proximity of these eigenstates to one another in terms of energy. Table I provides the overlap of the Koopman state and the ground-state of \tilde{H} , as well as the overlap between the Koopman state and the lowest-lying excited state with the same symmetry as the ground state ($^2S_{1/2}$ and $^2P_{3/2}$ for the alkali metal and halogen atoms, respectively). The rapid convergence behavior for the halogen atoms is easily rationalized by (i) the small overlap between the Koopman state and the lowest-energy excited $^2P_{3/2}$ symmetry state and (ii) the large energy gap between this state and the ground state (≈ 23 – 39 eV). We can see that the rate of convergence follows the degree of overlap in the sense that a large overlap with the excited state leads to slower convergence. On the other hand,

for the alkali metal atoms, the lowest-lying $^2S_{1/2}$ symmetry states are much closer in energy to the ground state ($\approx 2.5\text{--}4.2$ eV), and the degree of overlap with the Koopman states is significantly larger in the cases of K and Rb. As for the halogen atoms, the rate of convergence correlates with the overlap, with Na displaying the most rapid convergence, followed by Rb and K, in that order, with much slower convergence.

Figure 2 illustrates spectra for the alkali metal and halogen atoms derived from real-time TD-EA/IP-EOMCCSD simulations, with initial states prepared by imaginary-time simulations of various durations, as well as Lorentzian-broadened oscillator strengths taken from standard, frequency-domain EA/IP-EOMCCSD calculations. The spectra are normalized such that the most-intense feature in the energy range depicted has an intensity of one; a similar figure considering a wider energy range can be found in the Supporting Information. We can see that all features visible in Fig. 2 blue shift with increasing imaginary-time simulation length, τ . This behavior reflects the convergence of the ground-state energy, $E_0^{(N\pm 1)}$, that enters the propagator for the real-time simulation. Consistent with the data in Fig. 1, the absolute peak positions are visually well-converged within $\tau = 10.0$ a.u. As mentioned earlier, the approximate nature of $E_0^{(N\pm 1)}$ does not impact the relative peak positions, and the data presented in Fig. 2 are in line with this expectation. While relative peak intensities could be sensitive to the quality of the initial state preparation, it is difficult to discern any meaningful errors in peak heights from Fig. 2 at the scale of the figure.

We assess the impact of initial state quality on relative peak intensities, focusing on zero-field splitting features in these spectra. For the alkali metals, we consider the $^2S_{1/2}[ns^1] \rightarrow ^2P_{1/2}, ^2P_{3/2}[np^1]$ transitions, whereas for the halogens we consider $^2P_{3/2}[np^5] \rightarrow ^2D_{3/2}, ^2D_{5/2}[np^4(n+1)s^1]$. The ratios of the intensity of the lower-energy peak to that of the higher-energy one for each system are reported in Table II. The data indicate that even using the Koopman ($\tau = 0.0$ a.u.) state yields reasonable peak intensity ratios. For Na, K, and Rb, the percent errors in the ratios are all less than 2.0%. We observe larger errors in the peak intensities for the halogen atoms (5.4%, 3.5%, and 7.8% error, respectively, for F, Cl, and Br). These errors rapidly decrease with refinement of the initial state. After only 2.5 a.u. of imaginary time evolution, the percent error in the peak intensity ratios for all species drop to $\approx 0.2\%$ or lower. We note that some small residual error persists after 10.0 a.u. of imaginary time evolution (less than 0.005%), which we suspect is simply a numerical artifact.

V. CONCLUSIONS

We have presented a time-dependent extension of the EA/IP-EOMCC theory of open-shell systems, incorporating relativistic effects via the X2C formalism. This TD-EA/IP-EOMCC framework enables direct access to linear absorption spectra without the need for iterative diagonalization of the similarity-transformed Hamiltonian as an alternative route to frequency-domain EOMCC calculations.

TABLE II. Peak height ratios (lower-energy/higher-energy) characterizing the $^2S_{1/2}[ns^1] \rightarrow ^2P_{1/2}, ^2P_{3/2}[np^1]$ transitions in alkali metals and $^2P_{3/2}[np^5] \rightarrow ^2D_{3/2}, ^2D_{5/2}[np^4(n+1)s^1]$ transitions in halogens as functions of the imaginary time τ . The $\tau = \infty$ data in each atom correspond to the results obtained from frequency-domain EA/IP-EOMCCSD calculation. Errors in height ratio are reported as percentage relative to the $\tau = \infty$ values. The total real-time propagation time for these calculations is 671000 a.u..

Atom	τ (a.u.)	Peak height ratio	error in height ratio
Na	0.0	0.50529	0.0252%
	2.5	0.50514	0.0050%
	5.0	0.50514	0.0048%
	7.5	0.50514	0.0046%
	10.0	0.50514	0.0045%
	∞	0.50516	—
K	0.0	0.49615	0.0734%
	2.5	0.49651	0.0006%
	5.0	0.49649	0.0048%
	7.5	0.49649	0.0046%
	10.0	0.49649	0.0040%
	∞	0.49651	—
Rb	0.0	0.48093	1.0975%
	2.5	0.48585	0.0869%
	5.0	0.48622	0.0095%
	7.5	0.48627	0.0006%
	10.0	0.48627	0.0004%
	∞	0.48627	—
F	0.0	0.15627	5.3517%
	2.5	0.16508	0.0139%
	5.0	0.16511	0.0025%
	7.5	0.16511	0.0026%
	10.0	0.16511	0.0026%
	∞	0.16511	—
Cl	0.0	0.50090	3.4743%
	2.5	0.51871	0.0396%
	5.0	0.51892	0.0002%
	7.5	0.51892	0.0000%
	10.0	0.51892	0.0000%
	∞	0.51892	—
Br	0.0	1.34158	7.8489%
	2.5	1.45283	0.2072%
	5.0	1.45590	0.0033%
	7.5	1.45587	0.0011%
	10.0	1.45585	0.0001%
	∞	1.45585	—

We have shown that a Koopman determinant constructed by adding or removing a single electron from a closed-shell reference can serve as an effective starting point for real-time propagation for open-shell atomic systems (as opposed to the “exact” initial state, which is the lowest-energy eigenfunction of \hat{H} in the $(N \pm 1)$ -electron manifold). The primary difference between spectra resulting from the use of the Koopman initial state and the frequency-domain EA/IP-EOMCCSD results is a uniform shift, which rapidly decreases when the initial state is refined via evolution in imaginary time. The imaginary time propagation is a numerically inexpensive and conceptually straightforward alternative to traditional Davidson diagonalization for obtain the exact initial state. Like the uni-

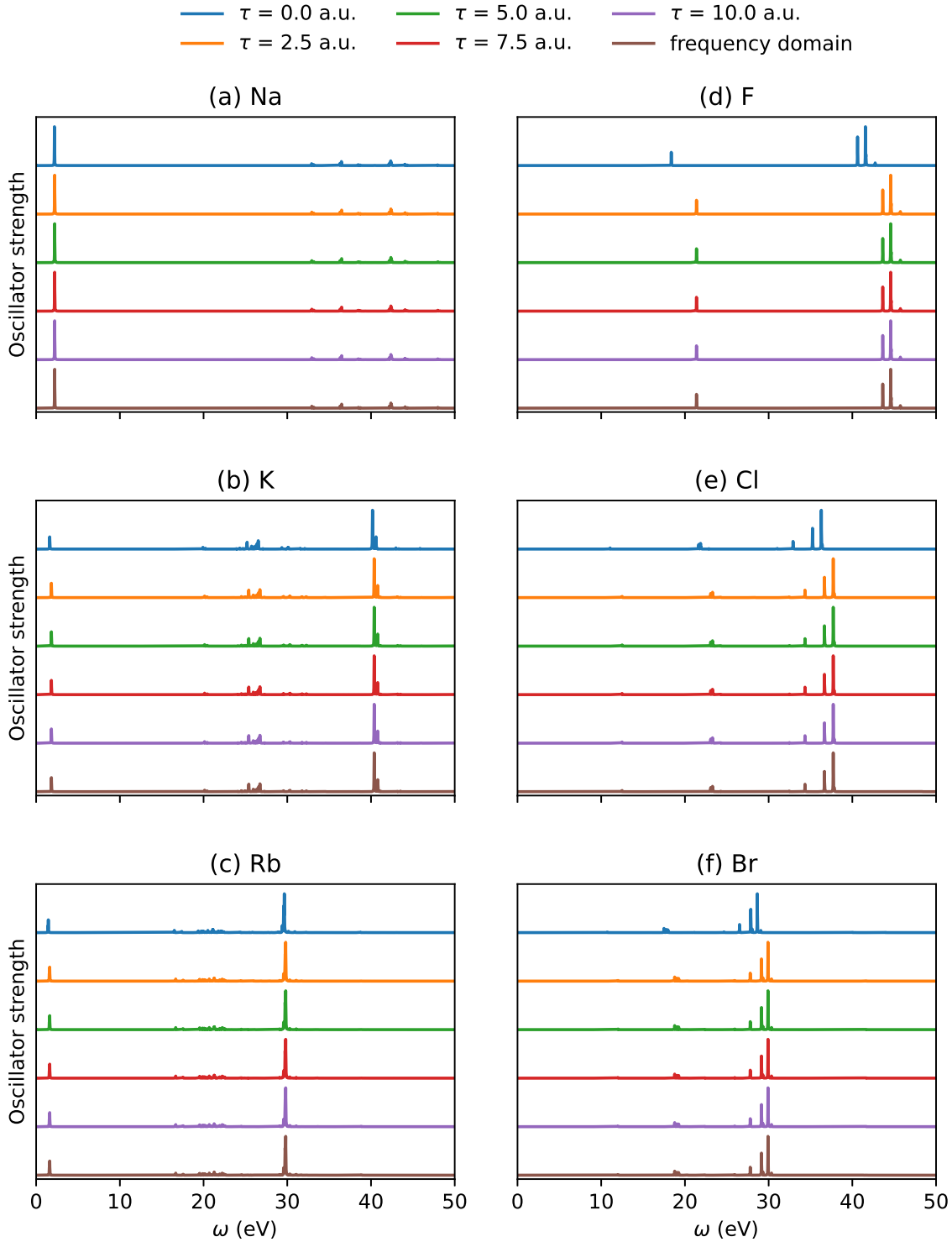


FIG. 2. Real-time spectrum obtained from Koopman state ($\tau = 0.0$, in blue), imaginary propagated states at $\tau = 2.5, 5.0, 7.5$ and 10.0 (in orange, green, red and purple respectively) and the frequency domain spectrum (in brown) for alkali metals and halogens. The peak heights are normalized to the highest intensity peak within the range $0 - 50$ eV. For all the atoms except for F, the peak with the highest intensity is situated within the range from $0 - 50$ eV. The peak with the highest intensity for F is situated ≈ 107.5 eV (see Fig. S2 in Supporting Information).

form shift, we have shown that peak intensity ratios associated with zero-field splitting features also approach the correct values as the initial state is refined.

Supporting Information Energy convergence for imaginary time propagation of alkali metal atoms up to $\tau = 100.0$ a.u., broad-band TD-EA/IP-EOMCCSD linear absorption spectra, overlaps between approximate initial states at various τ and eigenstates of \tilde{H} , and peak intensity ratios for zero-field splitting features.

ACKNOWLEDGMENTS

This material is based upon work supported by the National Science Foundation under Grant No. OAC-2103705. SHY acknowledges funding from the Quantum Initiative at Florida State University.

- ¹X. Li, N. Govind, C. Isborn, A. E. DePrince, and K. Lopata, *Chem. Rev.* **120**, 9951 (2020).
- ²B. S. Ofstad, E. Aurbakken, Ø. S. Schøyen, H. E. Kristiansen, S. Kvaal, and T. B. Pedersen, *WIREs Comput. Mol. Sci.*, e1666 (2023), Early View published online on May 1, 2023.
- ³F. Covito, E. Perfetto, A. Rubio, and G. Stefanucci, *Phys. Rev. A* **97**, 061401 (2018).
- ⁴J. B. Schriber and F. A. Evangelista, *J. Chem. Phys.* **151**, 171102 (2019).
- ⁵S. Lünnemann, A. I. Kuleff, and L. S. Cederbaum, *Chem. Phys. Lett.* **450**, 232 (2008).
- ⁶A. Bruner, S. Hernandez, F. Mauger, P. M. Abanador, D. J. LaMaster, M. B. Gaarde, K. J. Schafer, and K. Lopata, *J. Phys. Chem. Lett.* **8**, 3991 (2017).
- ⁷K. Lopata and N. Govind, *J. Chem. Theory Comput.* **7**, 1344 (2011).
- ⁸S. Tussupbayev, N. Govind, K. Lopata, and C. J. Cramer, *J. Chem. Theory Comput.* **11**, 1102 (2015).
- ⁹D. R. Nascimento and A. E. DePrince III, *J. Chem. Theory Comput.* **12**, 5834 (2016).
- ¹⁰C. Lian, M. Guan, S. Hu, J. Zhang, and S. Meng, *Adv. Theory Simul.* **1**, 1800055 (2018).
- ¹¹D. R. Nascimento and A. E. DePrince III, *J. Phys. Chem. Lett.* **8**, 2951 (2017).
- ¹²Y. C. Park, A. Perera, and R. J. Bartlett, *J. Chem. Phys.* **151**, 164117 (2019).
- ¹³J. J. Rehr, F. D. Vila, J. J. Kas, N. Y. Hirshberg, K. Kowalski, and B. Peng, *J. Chem. Phys.* **152**, 174113 (2020).
- ¹⁴F. D. Vila, J. J. Rehr, J. J. Kas, K. Kowalski, and B. Peng, *J. Chem. Theory Comput.* **16**, 6983 (2020).
- ¹⁵Y. C. Park, A. Perera, and R. J. Bartlett, *J. Chem. Phys.* **155**, 094103 (2021).
- ¹⁶F. D. Vila, K. Kowalski, B. Peng, J. J. Kas, and J. J. Rehr, *J. Chem. Theory Comput.* **18**, 1799 (2022).
- ¹⁷T. Moitra, L. Konecny, M. Kadek, A. Rubio, and M. Repisky, *J. Phys. Chem. Lett.* **14**, 1714 (2023).
- ¹⁸J. J. Goings and X. Li, *J. Chem. Phys.* **144**, 234102 (2016).
- ¹⁹S. Sun, R. Beck, D. B. Williams-Young, and X. Li, *J. Chem. Theory Comput.* **15**, 6824 (2019).
- ²⁰D. R. Nascimento and A. E. DePrince, III, *J. Chem. Phys.* **151**, 204107 (2019).
- ²¹Y. Zhang, J. D. Biggs, D. Healion, N. Govind, and S. Mukamel, *J. Chem. Phys.* **137**, 194306 (2012).
- ²²S. A. Fischer, C. J. Cramer, and N. Govind, *J. Chem. Theory Comput.* **11**, 4294 (2015).
- ²³J. Walkenhorst, U. De Giovannini, A. Castro, and A. Rubio, *Eur. Phys. J. B* **89**, 128 (2016).
- ²⁴T. S. Nguyen, J. H. Koh, S. Lefelhocz, and J. Parkhill, *J. Phys. Chem. Lett.* **7**, 1590 (2016).
- ²⁵M. Chen and K. Lopata, *J. Chem. Theory Comput.* **16**, 4470 (2020).
- ²⁶A. S. Skeidsvoll, T. Moitra, A. Balbi, A. C. Paul, S. Coriani, and H. Koch, *Phys. Rev. A* **105**, 023103 (2022).
- ²⁷F. Coester, *Nucl. Phys.* **7**, 421 (1958).
- ²⁸F. Coester and H. Kümmel, *Nucl. Phys.* **17**, 477 (1960).
- ²⁹J. Čížek, *J. Chem. Phys.* **45**, 4256 (1966).
- ³⁰J. Čížek, *Adv. Chem. Phys.* **14**, 35 (1969).
- ³¹J. Paldus, J. Čížek, and I. Shavitt, *Phys. Rev. A* **5**, 50 (1972).
- ³²J. Paldus and X. Li, *Adv. Chem. Phys.* **110**, 1 (1999).
- ³³R. J. Bartlett and M. Musiał, *Rev. Mod. Phys.* **79**, 291 (2007).
- ³⁴K. Emrich, *Nucl. Phys. A* **351**, 379 (1981).
- ³⁵J. Geertsen, M. Rittby, and R. J. Bartlett, *Chem. Phys. Lett.* **164**, 57 (1989).
- ³⁶J. F. Stanton and R. J. Bartlett, *J. Chem. Phys.* **98**, 7029 (1993).
- ³⁷G. D. Purvis and R. J. Bartlett, *J. Chem. Phys.* **76**, 1910 (1982).
- ³⁸J. M. Cullen and M. C. Zerner, *J. Chem. Phys.* **77**, 4088 (1982).
- ³⁹M. R. Hoffmann and H. F. Schaefer, *Adv. Quantum Chem.* **18**, 207 (1986).
- ⁴⁰J. Noga and R. J. Bartlett, *J. Chem. Phys.* **86**, 7041 (1987), **89**, 3401 (1988) [Erratum].
- ⁴¹G. E. Scuseria and H. F. Schaefer, *Chem. Phys. Lett.* **152**, 382 (1988).
- ⁴²J. D. Watts and R. J. Bartlett, *J. Chem. Phys.* **93**, 6104 (1990).
- ⁴³N. Oliphant and L. Adamowicz, *J. Chem. Phys.* **95**, 6645 (1991).
- ⁴⁴S. A. Kucharski and R. J. Bartlett, *Theor. Chem. Acc.* **80**, 387 (1991).
- ⁴⁵S. A. Kucharski and R. J. Bartlett, *J. Chem. Phys.* **97**, 4282 (1992).
- ⁴⁶P. Piecuch and L. Adamowicz, *J. Chem. Phys.* **100**, 5792 (1994).
- ⁴⁷C. Huber and T. Klamroth, *J. Chem. Phys.* **134**, 054113 (2011).
- ⁴⁸T. B. Pedersen and S. Kvaal, *J. Chem. Phys.* **150**, 144106 (2019).
- ⁴⁹H. E. Kristiansen, Ø. S. Schøyen, S. Kvaal, and T. B. Pedersen, *J. Chem. Phys.* **152**, 071102 (2020).
- ⁵⁰A. S. Skeidsvoll and H. Koch, *Phys. Rev. A* **108**, 033116 (2023).
- ⁵¹S. Kvaal, *J. Chem. Phys.* **136**, 194109 (2012).
- ⁵²T. Sato, H. Pathak, Y. Orimo, and K. L. Ishikawa, *J. Chem. Phys.* **148**, 051101 (2018).
- ⁵³H. Pathak, T. Sato, and K. L. Ishikawa, *J. Chem. Phys.* **152**, 124115 (2020).
- ⁵⁴H. Pathak, T. Sato, and K. L. Ishikawa, *J. Chem. Phys.* **153**, 034110 (2020).
- ⁵⁵H. Pathak, T. Sato, and K. L. Ishikawa, *J. Chem. Phys.* **154**, 234104 (2021).
- ⁵⁶A. Köhn and J. Olsen, *J. Chem. Phys.* **122**, 084116 (2005).
- ⁵⁷J. A. Sonk, M. Caricato, and H. B. Schlegel, *J. Phys. Chem. A* **115**, 4678 (2011).
- ⁵⁸E. Luppi and M. Head-Gordon, *Mol. Phys.* **110**, 909 (2012).
- ⁵⁹L. N. Koulias, D. B. Williams-Young, D. R. Nascimento, A. E. DePrince III, and X. Li, *J. Chem. Theory Comput.* **15**, 6617 (2019).
- ⁶⁰B. C. Cooper, L. N. Koulias, D. R. Nascimento, X. Li, and A. E. DePrince III, *J. Phys. Chem. A* **125**, 5438 (2021).
- ⁶¹R. J. Bartlett and J. F. Stanton, in *Reviews in Computational Chemistry* (John Wiley & Sons, Ltd, 1994) pp. 65–169.
- ⁶²M. Nooijen and J. G. Snijders, *Int. J. Quantum Chem.* **44**, 55 (1992).
- ⁶³M. Nooijen and J. G. Snijders, *Int. J. Quantum Chem.* **48**, 15 (1993).
- ⁶⁴J. F. Stanton and J. Gauss, *J. Chem. Phys.* **101**, 8938 (1994).
- ⁶⁵M. Musiał, S. A. Kucharski, and R. J. Bartlett, *J. Chem. Phys.* **118**, 1128 (2003).
- ⁶⁶M. Musiał and R. J. Bartlett, *Chem. Phys. Lett.* **384**, 210 (2004).
- ⁶⁷Y. J. Bomble, J. C. Saeh, J. F. Stanton, P. G. Szalay, M. Kállay, and J. Gauss, *J. Chem. Phys.* **122**, 154107 (2005).
- ⁶⁸J. R. Gour, P. Piecuch, and M. Włoch, *J. Chem. Phys.* **123**, 134113 (2005).
- ⁶⁹J. R. Gour, P. Piecuch, and M. Włoch, *Int. J. Quantum Chem.* **106**, 2854 (2006).
- ⁷⁰J. R. Gour and P. Piecuch, *J. Chem. Phys.* **125**, 234107 (2006).
- ⁷¹M. Nooijen and R. J. Bartlett, *J. Chem. Phys.* **102**, 3629 (1995).
- ⁷²M. Nooijen and R. J. Bartlett, *J. Chem. Phys.* **102**, 6735 (1995).
- ⁷³M. Musiał and R. J. Bartlett, *J. Chem. Phys.* **119**, 1901 (2003).
- ⁷⁴N. C. Rubin and A. E. D. III, *Mol. Phys.* **119**, e1954709 (2021).
- ⁷⁵M. D. Liebenthal, S. H. Yuwono, L. N. Koulias, R. R. Li, N. C. Rubin, and A. E. I. DePrince, *J. Phys. Chem. A* **129**, 6679 (2025).
- ⁷⁶D. B. Williams-Young, A. Petrone, S. Sun, T. F. Stetina, P. Lestrage, C. E. Hoyer, D. R. Nascimento, L. Koulias, A. Wildman, J. Kasper, J. J. Goings, F. Ding, A. E. DePrince III, E. F. Valeev, and X. Li, *WIREs Comput. Mol. Sci.* **10**, e1436 (2020).
- ⁷⁷D. G. A. Smith, L. A. Burns, A. C. Simmonett, R. M. Parrish, M. C. Schieber, R. Galvelis, P. Kraus, H. Kruse, R. Di Remigio, A. Alenaizan, A. M. James, S. Lehtola, J. P. Misiewicz, M. Scheurer, R. A. Shaw, J. B. Schriber, Y. Xie, Z. L. Glick, D. A. Sirianni, J. S. O'Brien, J. M. Waldrop,

- A. Kumar, E. G. Hohenstein, B. P. Pritchard, B. R. Brooks, H. F. Schaefer, A. Y. Sokolov, K. Patkowski, A. E. DePrince, U. Bozkaya, R. A. King, F. A. Evangelista, J. M. Turney, T. D. Crawford, and C. D. Sherrill, *J. Chem. Phys.* **152**, 184108 (2020).
- ⁷⁸P. Piecuch, S. A. Kucharski, K. Kowalski, and M. Musiał, *Comput. Phys. Commun.* **149**, 71 (2002).
- ⁷⁹F. Zahariev, P. Xu, B. M. Westheimer, S. Webb, J. Galvez Vallejo, A. Tiwari, V. Sundriyal, M. Sosonkina, J. Shen, G. Schoendorff, M. Schlinsog, T. Sattasathuchana, K. Ruedenberg, L. B. Roskop, A. P. Rendell, D. Poole, P. Piecuch, B. Q. Pham, V. Mironov, J. Mato, S. Leonard, S. S. Leang, J. Ivanic, J. Hayes, T. Harville, K. Gururangan, E. Guidez, I. S. Gerasimov, C. Friedl, K. N. Ferreras, G. Elliott, D. Datta, D. D. A. Cruz, L. Carrington, C. Bertoni, G. M. J. Barca, M. Alkan, and M. S. Gordon, *J. Chem. Theory Comput.* **19**, 7031 (2023).
- ⁸⁰P. Pollak and F. Weigend, *J. Chem. Theory Comput.* **13**, 3696 (2017).
- ⁸¹B. P. Pritchard, D. Altarawy, B. Didier, T. D. Gibson, and T. L. Windus, *J. Chem. Inf. Model.* **59**, 4814 (2019).